ETH zürich

ETH Library

Application of Twyman-Green interferometers for shock-containing free jets from axisymmetric convergent micro nozzles

Conference Paper

Author(s):
Sugawara, S.; Nakao, S.; Miyazato, Y.; Ishino, Y.

Publication date:
2018-10-05

Permanent link:
https://doi.org/10.3929/ethz-b-000279229

Rights / license:
In Copyright - Non-Commercial Use Permitted

This page was generated automatically upon download from the ETH Zurich Research Collection.
For more information, please consult the Terms of use.

APPLICATION OF TWYMAN-GREEN INTERFEROMETERS FOR SHOCK-CONTAINING FREE JETS FROM AXISYMMETRIC CONVERGENT MICRO NOZZLES

S. Sugawara [1], S. Nakao [1], Y. Miyazato [1,c], and Y. Ishino [2]

[1] Department of Mechanical Systems Engineering, The University of Kitakyushu,
1-1 Hibikino, Wakamatsu-ku, Kitakyushu, Fukuoka, 808-0135, Japan
[2] Department of Mechanical Engineering, Nagoya Institute Technology,
Gokiso-cho, Showa-ku, Nagoya, Aichi, 466-8555, Japan
[c]Corresponding author: Tel.: +81936953219; Email: miyazato@kitakyu-u.ac.jp

KEYWORDS:
Main subjects: flow visualization, RANS simulation, microjet
Fluid: shock-containing flow, Underexpanded free jet
Visualization method(s): Twyman-Green interferometer
Other keywords: axisymmetric convergent nozzle

ABSTRACT: *In the present study, the Twyman-Green interferometer using the wedge fringe method is applied for the first time to measure the underexpanded free jet emitted from a micro convergent nozzle in order to provide reliable experimental data, which can subsequently be utilized as a suitable benchmark validation for Reynolds-Averaged Navier-Stokes (RANS) simulations of shock-containing jets. An interferogram analysis for reconstructing the jet density fields is performed using the Nestor-Olsen algorithm for the Abel inversion under the assumption of axial symmetry in the flow and the Fourier-transform method for the analysis of the phase shift of the deformed fringe relative to the background fringe. RANS simulations with the SST k-ω turbulent model are also carried out for a quantitative mutual comparison with other experiments. A spatial variation of a shock-containing microjet is clearly displayed in the density contour plot at the cross-sectional area, including the jet centerline as well as the streamwise and radial density profiles. Additionally, the density profile along the jet centerline obtained by the present Twyman-Green interferometer system is quantitatively compared with those from past quantitative visualization studies, including the rainbow schlieren deflectometry, the background oriented schlieren, the moiré schlieren, and the Mach-Zehnder interferometer.*

1 Introduction

In recent years, there has been considerable research on the subject of the dynamics of a supersonic microjet for the application of microscale devices, including a small satellite thruster in space engineering [1], a critical nozzle for obtaining mass-flow rate at a low Reynolds number [2], and a micro-propulsion nozzle [3]. A deep, detailed comprehension of the flow characteristics through such devices requires information regarding the quantitative velocity, density, and temperature measurements in the flow field. However, until recently, there has been very little experimental data on supersonic microjets available in the literature. The structure of supersonic microjets was studied for the first time by Scroggs and Settles [4], who made axisymmetric nozzles with exit Mach numbers ranging from 1.0 to 2.8 and two different inner diameters of 600 μm and 1200 μm at the nozzle exit. They measured the Pitot pressures along the jet centerline by impinging the jet upon a flat plate, including a pressure port of 0.2 mm in diameter with a pressure sensor attached to the reverse side. Phalnikar et al. [5] fabricated a micro Pitot probe with a pressure hole of 50 μm in diameter, and later, Aniskin et al. [6] developed one with an intake port of 12 μm diameter. These two groups performed the Pitot pressure measurements to study the size of shock cells and the supersonic core length of the microjet. However, the intrusive probe, including a Pitot probe, a static pressure tube, and a hot-wire anemometer, can measure the flow parameters only at discrete

points and such probes are very sensitive to the flow alignment [7]. In addition, such an intrusive probe could alter the flow fields by the presence of the probe located inside the flow. However, nonintrusive techniques such as the Laser Doppler and the Particle Image Velocimetry can be used for velocity measurements. However, these techniques often contain an inherent error such that tracer particles cannot follow a strong velocity gradient across a shock wave. Therefore, with complex shock-containing structures, a proper and homogeneous seeding is very difficult [8 ~ 10]. For a supersonic free jet operating at slightly off-design conditions, several analytical models predicting the flow properties inside a jet plume have been proposed [11 ~ 16]. However, no exact solutions exist for a supersonic free jet with strong shock waves such as Mach disks and barrel shocks, or shock wave-vortex interactions.

As a computational fluid dynamic (CFD) analytical tool, RANS has been used to provide reasonably accurate results within a relatively short period of time, and applied to various engineering applications [17, 18]. However, it is noted that these numerical models are not "closed" in the sense that they rely on additional physical approximations (for instance, a turbulence model needs a closure model for the Reynolds stress and makes use of model parameters, which need to be adjusted depending on flow characteristics such as the Mach number, Reynolds number, etc.) Therefore, it is critical that the capability of these models is assessed before the numerical results are accepted. To validate a computational model, reliable experimental data are important. One method for useful validation for numerical simulations of microjet pressure measurement data is by obtaining it through use of a Pitot probe, which has been widely used thus far [19 ~ 21].

Also, a conventional flow visualization such as the schlieren and shadowgraph techniques [22] has been routinely used [23]. However, quantitative measurements of some physical properties (e.g., temperature, density, pressure, and velocity fields) are not available, and thus, these measurements are used to validate a computational model by examining the qualitative difference observed in calculated geometrical features such as position, length and shape of shock waves [23 ~ 25].

In the present study, an axisymmetric convergent nozzle with an inner diameter of 1 mm at its exit is used as a first step for obtaining three-dimensional density fields of a supersonic microjet showing complex shock structures. To this aim, the Twyman-Green interferometer [26], which is known as a modification of the Michelson interferometer, is utilized to investigate shock-containing microjets, which may be useful in the CFD community for the validation data of their numerical simulations of shock-containing microjets. In addition, we study, both experimentally and numerically, the free jet under the same operating conditions. The results obtained by RANS with the SST k-ω turbulent model are compared with the experimental data, and the spatial variations of the free jet flow fields are examined. Also presented here is a quantitative comparison between our experimental data and data using the following past quantitative visualization methods: the rainbow schlieren deflectometry, the background oriented schlieren, the moiré schlieren, and the Mach-Zehnder interferometer.

2 Experimental apparatus

The experiments were conducted in a blowdown compressed-air facility of High-Speed Gasdynamics Laboratory at the University of Kitakyushu. A schematic diagram of the experimental apparatus with a laser interferometer system is shown in Fig. 1. The air supplied by a compressor that pressurizes the ambient air up to 1 MPa is filtered, dried and stored in a high-pressure reservoir consisting of two storage tanks with a total capacity of 2 m^3. The high-pressure dry air from the reservoir is stagnated in a plenum chamber shown in Fig. 1 and then discharged into the atmosphere through a test nozzle. In the present experiment, the plenum pressure is controlled and maintained constant during the testing by a solenoid valve. As schematically shown in Fig. 2, an axisymmetric convergent nozzle with a 6 mm and 1 mm in diameter at the inlet and exit, respectively, was used as the test nozzle. The nozzle wall contour from the inlet to exit was designed using a sinusoidal curve

so as to give smooth uniform flows at the inlet and exit. The experiment was carried out at a nozzle pressure ratio of NPR = 4.0 within an accuracy of ± 1.0% to produce an underexpanded free jet. The total temperature in the plenum chamber was equal to the room temperature within an accuracy of about 0.1 centigrade during the experiment. To obtain a density field in a shock-containing microjet, quantitative flow visualization was made using a Twyman-Green interferometer system with a field of view of 50 mm diameter. The Reynolds number Re_{De} at the nozzle exit is $Re_{De} = 6.16 \times 10^4$, which is calculated based on the assumption of the isentropic flow from the nozzle inlet to exit.

A Twyman-Green interferometer is an optical instrument of high precision and versatility which is schematically shown in Fig. 1 with the associated optical equipment where a blue semiconductor laser with a wavelength of 405 nm was utilized as a light source. The laser beam is expanded by a spatial filter to make a coherent beam before collimated into a parallel beam and is split into reference and test beams by a beamsplitter, which reflects roughly half of the intensity of the wave front in one direction and transmits the rest in another direction. The reference beam passes through still air and returns to the beamsplitter after reflection at Mirror 1. The test beam passes through a refracted index field produced by a free jet issued from a test nozzle and also returns to the beamsplitter after being reflected at Mirror 2. The two beams are combined before being focused by an imaging lens to produce interferograms on the recording medium in a digital camera.

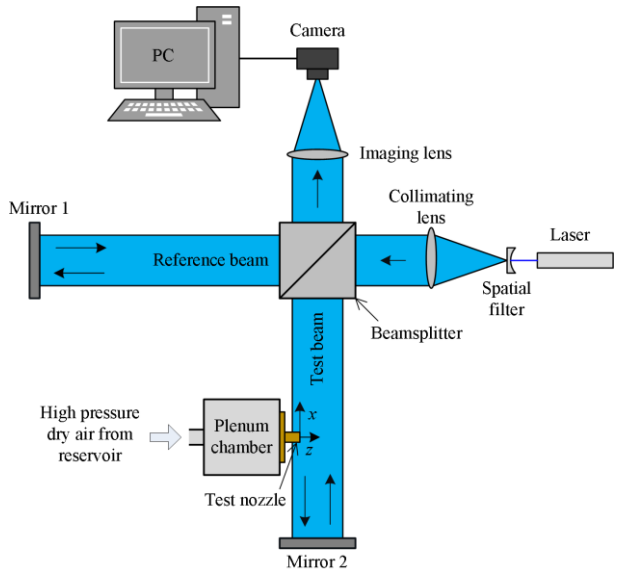

Fig. 1. Schematic of experimental apparatus

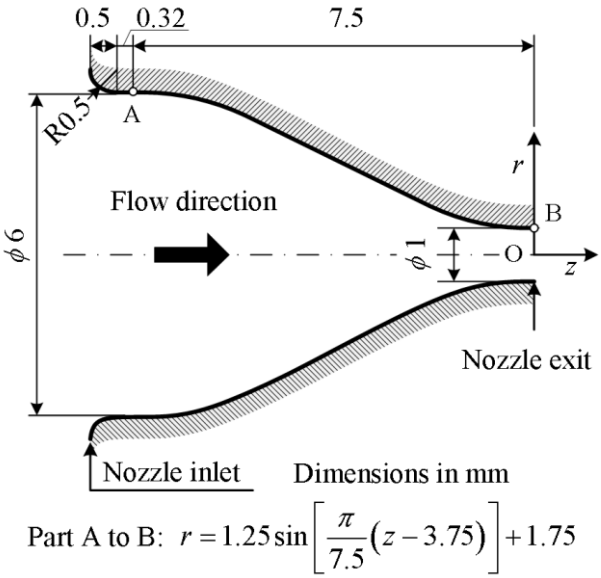

Fig. 2. Schematic of test nozzle

3 Reconstruction of jet density fields

The method for reconstructing a jet density field consists of two steps, which are the acquisition of the values of fringe shifts from their original positions measured in the experiment and the calculation of density values using the resulting fringe shifts. The former can be done using the Fourier transform method presented by Takeda et al. [27] and the latter by the Nestor-Olsen algorithm [28] for the Abel inversion method under the assumption of an axisymmetric density field. The methodology of extracting the density field using both of the methods is described below.

Generally, Twyman-Green interferometers can be arranged so as to produce wedge fringe and infinite fringe patterns. In the infinite fringe method, each fringe occurs due to one wavelength shift in the optical path length as a result of changes in the flow field [29]. The wedge fringe method can

measure densities more minutely than the infinite fringe method by analyzing a fringe shift, therefore, the wedge fringe method was employed in the present work. In the wedge fringe method, the mirrors and beam splitter are deliberately misaligned to produce an initial fringe pattern or a background fringe pattern of straight lines and image processing techniques are used for obtaining density fields by digital subtraction of the background fringe pattern from the deformed fringe pattern. In the present experiment, the background fringes were set in horizontal orientation with respect to the nozzle axis by appropriate adjustment of Mirror 2 shown in Fig. 1.

3.1 Fourier transform method

When the test beam is passing through the free jet with a variable refractive-index field, the background fringes are changed into deformed fringe patterns because of the phase shift caused by the variations of the light speed as the beam passes through the test field. On the recording medium of a digital camera for a fixed time, the typical profiles showing background and deformed fringe patterns are illustrated in Fig. 3 as lines of constant phase. The parallel and equally spaced fringes shown as blue solid lines in Fig. 3(a) are also referred to as wedge fringes. The interval b in Fig. 3(a) denotes the distance between two successive crests of the background fringes and it is a function of the intersection angle between the reference and test beams and the wavelength of the laser light used in the experiment. The red dashed line in Fig. 3(b) shows the intensity profile $g(y, z_0)$ corresponding to the deformed fringe pattern at a particular axial position z_0 and it can be given by [27, 30]

$$g(y, z_0) = g_0(y, z_0) + g_1(y, z_0)\cos[k_0 y - \Delta\varphi(y, z_0)] \tag{1}$$

with the phase shift $\Delta\varphi(y, z_0)$ containing the desired information on the density field in the free jet where $g_0(y, z_0)$ and $g_1(y, z_0)$ represent unwanted irradiance variations arising from the nonuniform light reflection or transmission when the test beam is passing through the free jet, and $k_0 = 2\pi/b$. The coordinates y and z form the vertical plane, which is perpendicular to the test beam propagation direction, and the x-axis is taken as the direction in which the test beam propagates after being reflected at Mirror 2 shown in Fig. 1.
Equation (1) can be rewritten in the following expression

$$g(y, z_0) = g_0(y, z_0) + c(y, z_0)\exp(ik_0 y) + c^*(y, z_0)\exp(-ik_0 y) \tag{2}$$

with

$$c(y, z_0) = \frac{1}{2} g_1(y, z_0)\exp[-i\Delta\varphi(y, z_0)] \tag{3}$$

where i is the imaginary unit and the asterisk * denotes the complex conjugate.
The Fourier transform of Eq. (2) with respect to y is given by

$$G(k, z_0) = G_0(k, z_0) + C(k - k_0, z_0) + C^*(k + k_0, z_0) \tag{4}$$

where the capital letters denote the Fourier transforms of the respective primitive functions and k is the spatial wave number in the y direction. Since the spatial variations of $g_0(y, z_0)$, $g_1(y, z_0)$, and $\Delta\varphi(y, z_0)$ are slow compared with the spatial frequency k_0 when the interval between fringes is sufficiently small, the Fourier spectra in Eq. (4) are separated by the wave number k_0 and have the three independent peaks, as schematically shown in Fig. 4(a). We make use of either of the two spectra on the carrier, say $C(k - k_0, z_0)$, and translate it by k_0 on the wave number axis toward the

origin to obtain $C(k, z_0)$, as shown in Fig. 4(b). The unwanted background variation $G_0(k, z_0)$ has been filtered out in this stage by a pertinent band pass filter.

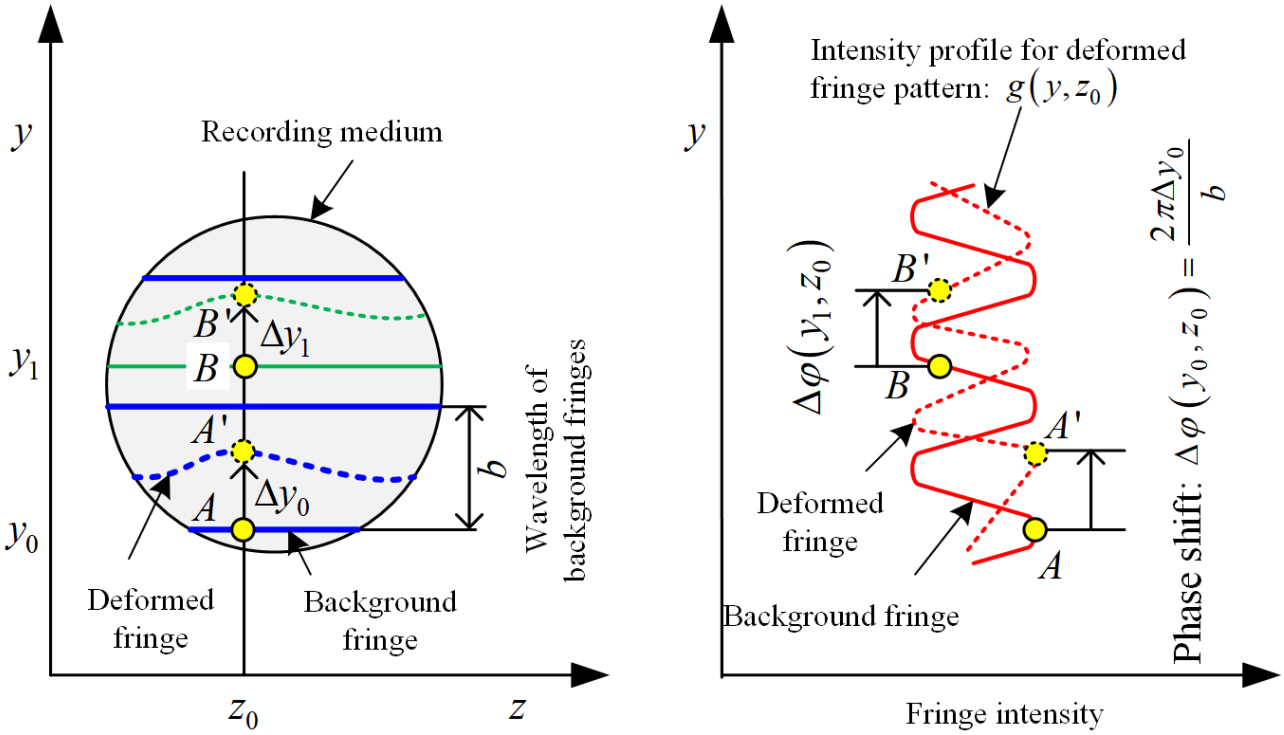

(*a*) Fringe patterns on recording medium (*b*) Fringe intensity profiles at $z = z_0$

Fig. 3. Variation of background and deformed fringes by wedge fringe method

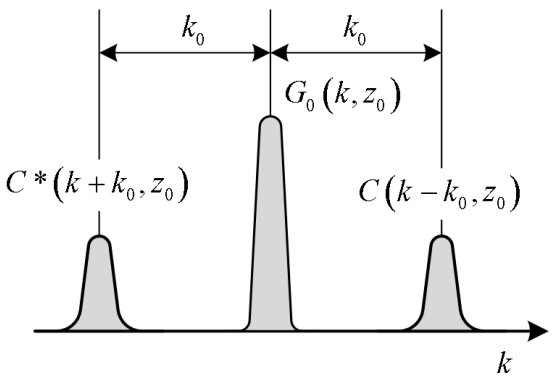

(a) Separated Fourier spectra

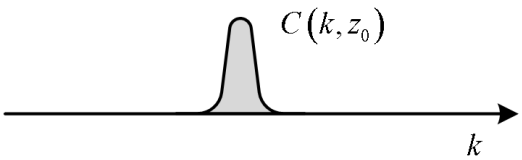

(b) Parallel translation of single spectrum selected

Fig. 4. Fourier-transform method for fringe-pattern analysis

Applying the inverse Fourier transform of $C(k, z_0)$ with respect to the k to obtain $c(y, z_0)$ defined by Eq. (3) and taking the logarithm of Eq. (3) leads to

$$\ln c(y, z_0) = \ln \frac{g_1(y, z_0)}{2} - i\Delta\varphi(y, z_0) \tag{5}$$

From Eq. (5), we can obtain the phase shift $\Delta\varphi(y, z_0)$ in the imaginary part completely separated from the unwanted amplitude variation $g_1(y, z_0)$ in the real part.

3.2 Abel inversion method

On a free jet with an axisymmetric refractive index field depicted in Fig. 5(a), the refractive index n in the flow field depends only on the radial distance r from the centerline O ($x = y = 0$) for a fixed axial distance z_0 measured from the nozzle exit plane, i.e.,

$$n = n(r, z_0), \quad for \quad 0 \le r \le R, \quad n = n_a, \quad for \quad R < r \tag{6}$$

where n_a is the refractive index for the ambient air and R the radial distance to the jet boundary.

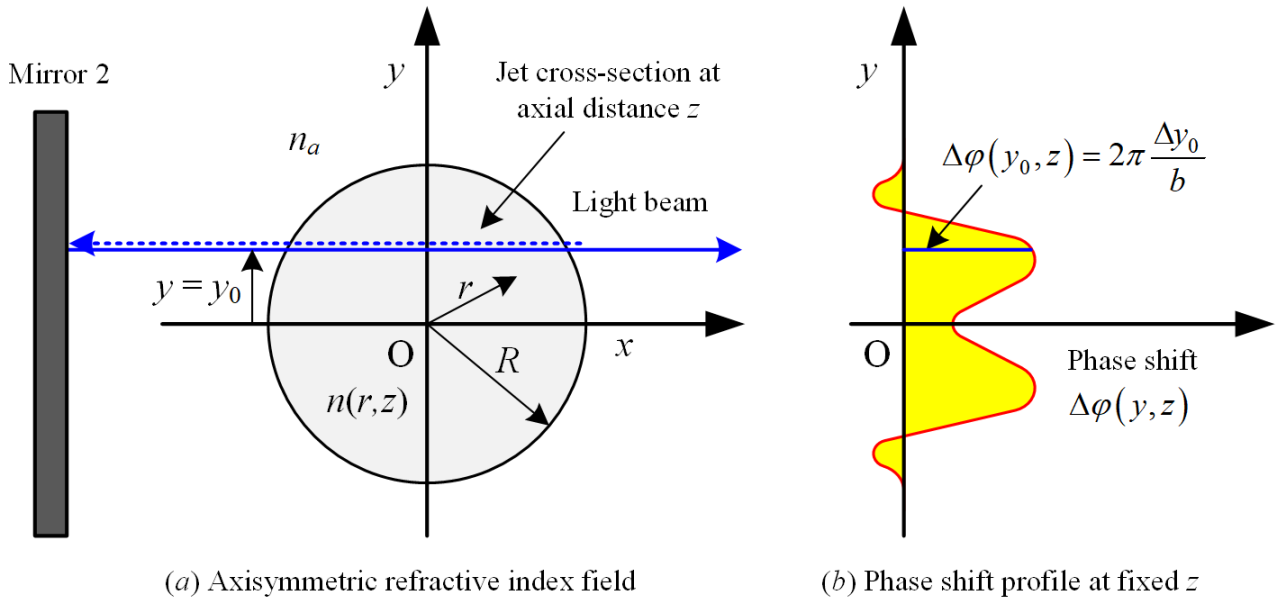

(a) Axisymmetric refractive index field (b) Phase shift profile at fixed z

Fig. 5. Light beam passing through axisymmetric refractive index field

Refractive index values can be obtained directly from the measured fringe positions on a given cross section normal to the jet axis, and each measured cross section is independent of others. As illustrated in Fig. 5(a), in the case of the Twyman-Green interferometer, the test beam passes through the refractive index field twice: One is the incident test beam travelling toward Mirror 2 and the other is the test beam after reflection at Mirror 2, which are denoted as the blue dashed and blue solid lines, respectively. Therefore, the optical path-length difference $OPL(y, z_0)$ of the test beam which passed through the field with and without the jet, can be expressed by

$$OPL(y, z_0) = 4\int_y^R \frac{\left[n(r, z_0) - n_a\right]}{\sqrt{r^2 - y^2}} r dr \tag{7}$$

The fringe shift Δy at any location on a recording medium can be related to the $OPL(y, z_0)$ as follows:

$$\Delta y = \frac{b}{\lambda_0} OPL(y, z_0) \tag{8}$$

where λ_0 is the wavelength of light in vacuum for the laser used. Also, the use of the Gradstone-Dale relation

$$n(r,z) = 1 + K\rho(r,z) \tag{9}$$

with combination of Eqs. (7) and (8) gives

$$\Delta y = \frac{4bK}{\lambda_0} \int_y^R \frac{\left[\rho(r,z_0) - \rho_a\right]}{\sqrt{r^2 - y^2}} r dr \tag{10}$$

where K is the Gradstone-Dale constant and ρ_a is the density of ambient air.
Once the fringe shifts for a fixed streamwise location z_0 are obtained by the Fourier transform method, the density field is found by inverting Eq. (10) using the Abel inversion [31]:

$$\rho(r,z_0) = \rho_a - \frac{\lambda_0}{2\pi bK} \int_r^R \frac{\frac{d}{dy}(\Delta y)}{\sqrt{y^2 - r^2}} dy \tag{11}$$

Measurements of the fringe shifts provide only a discrete set of values, therefore, Eq. (11) can only be solved numerically. Several algorisms for solving the Abel-inversion equation have been proposed so far [28, 32 ~ 36], and the integral in Eq. (11) can be evaluated by using the Nester-Olsen algorithm [28] as follows:

$$\rho(r_k, z_0) = \rho_a - \frac{\lambda_0}{\pi K \Delta w} \sum_{n=k}^{N} B_{k,n} \left(\frac{\Delta y}{b}\right)_n \tag{12}$$

where $r_k = k\Delta w$ ($k = 0, 1, 2, ..., N$) is the radial distance from the jet centerline, Δw is the sampling interval which is the same as the distance between neighboring pixels on the recording medium, N is the total number of intervals in the medium, and

$$B_{k,n} = -A_{k,n} \quad if \quad n = k, \qquad B_{k,n} = A_{k,n-1} - A_{k,n} \quad if \quad n \geq k+1 \tag{13}$$

with

$$A_{k,n} = \frac{\sqrt{(n+1)^2 - k^2} - \sqrt{n^2 - k^2}}{2n+1} \tag{14}$$

Density values can capture at the spatial resolution determined by the sampling interval. Interferogram images of a free jet obtained by the Twyman-Green interferometer were recorded in 30 pictures at a sampling frequency of 10 kHz and formed onto a CMOS camera (The Imaging

Source, DFK72BUC02) which recorded a JPEG RGB image (24-bit each color) at a resolution of 2592×1944 square pixels. The plane of focus was located in the nozzle axis. The RGB image was then turned into an 8-bit grayscale image by a linear transformation. Therefore, the distributions of background and deformed fringes with 256 different possible intensities can be calculated from the Twyman-Green interferometer for the density-field in the free jet. The effective spatial resolution of the present imaging system is around 4 μm/pixel. The average and standard deviation for the experiment were obtained over the 30 samples recorded in the experiment.

4 Numerical methods

The jet flow issued from an axisymmetric convergent nozzle with inner diameter (D_e) 1 mm at the nozzle exit is calculated using the commercial CFD software ANSYS Fluent Version 15.0. Figure 6(a) shows a schematic drawing of the computational domain and a coordinate system of the present numerical simulation. The center on the nozzle exit plane is taken as the origin (i.e., $z = 0$ and $r = 0$, where z-axial direction and r-radial direction). The flow is assumed to be symmetric with respect to the z-axis; therefore, only the upper half of the domain needs to be considered. The axisymmetric pressure-based compressible RANS equations are numerically solved. In the present simulation, the turbulent model turns on due to the fact that the Reynolds number based on D_e is 6.16×10^4, which is much higher than that which is presented in the experimental data of Nakao and Takamoto [2]. In their experiment, choked flows through the Laval-typed and convergent-typed nozzles are considered, and it is observed that a transition from laminar to turbulent flow in boundary layers occurs at a throat Reynolds number of ~10,000. Menter's SST k-ω turbulent model is employed in the present study because of its robustness for a variety of CFD applications, including transonic and supersonic flows as well as shock-wave-boundary layer interactions [18].

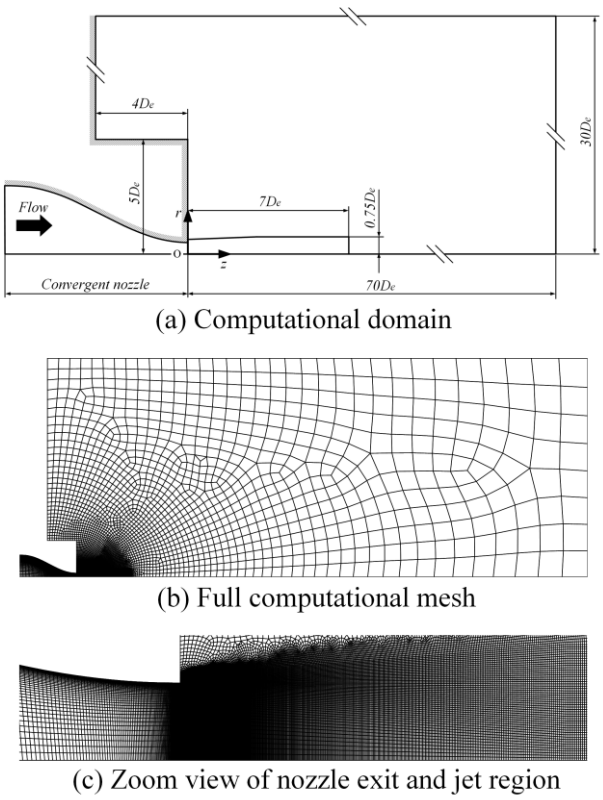

(a) Computational domain

(b) Full computational mesh

(c) Zoom view of nozzle exit and jet region

Fig. 6. Computational domain and boundary conditions

The inlet and ambient conditions are identical to the experimental setup in that the plenum pressure (p_{os}) and temperature upstream of the nozzle are 404 kPa and 300 K, respectively, and the back pressure (p_b) is set to the atmospheric pressure, 101 kPa. Thus, the nozzle operating pressure ratio, p_{os}/p_b, is kept constant at 4.0. The dry air is assumed to follow the perfect gas law with a constant specific heat ratio of γ = 1.4, and the coefficient of viscosity is calculated by using Sutherland's formula. Figures 6(b) and 6(c) show the meshes of the entire computational domain and near the nozzle exit, respectively. The solid walls including the nozzle wall are treated as adiabatic and no-slip, and the top and right boundaries are the pressure outlets (i.e., p_b is specified). The structured mesh is generated by the mapped face meshing function equipped with ANSYS Fluent and the total mesh count is approximately 50 thousand elements. The grid spacing in the z-direction within the region from z = 0 to $7D_e$ is relatively uniform and very fine in order to resolve the complex shock structures. Inside the nozzle, the grid size smoothly decreases in the radial direction to capture the boundary layer. To capture the fine structures of shock-containing microjets, we set a minimum mesh interval to ~2 μm in the vicinity of the nozzle exit. (Note that the spatial measurement resolution of the density is around 4 μm.)
The number of iterations is 10,000, at which the residuals of all equations (species, momentum, energy, turbulent kinetic energy, k, and ω) reduce by an order of three and the solutions seem to sufficiently converge. Here, the CFL number is set to be small (= 0.1) due to the fact that a large CFL number results in the undesired oscillation of the shock fronts and thus, the overall computational time increases. We use the differentiable function as the limiter of the MUSCL scheme to achieve the third-order accuracy in space. Note that using the high-order scheme, which satisfies a total-variation-diminishing (TVD) condition, is particularly important for this type of application. The time integration is performed using the three-stage Runge-Kutta method.
It should be noted that, as seen during the experiment, there are some unsteady motions that are overlooked in this steady calculation. Thus, a high-fidelity numerical simulation, such as a Large-Eddy Simulation (LES), should be explored to capture unsteady features. (Please cite the recent LES simulation by Li, X., Zhou, et al. [25])

5 Results and Discussion

Figure 7(a) shows an interferogram of an axisymmetric underexpanded microjet (the flow direction is left-to-right) in which the ratio of the plenum pressure to the back pressure is kept constant at NPR = 4.0 in such a manner that the nozzle is operated at an underexpanded condition. The shock-cell structures can be faintly visible in the jet plume. Parts A and B, enclosed by a red quadrangle in Fig. 7(a), are the regions: one is far from the jet plume, and the one other includes the reflected shock in the first shock cell. Figure 7(b) (an enlarged view of Part A in Fig. 7(a)) represents an image of the background fringe pattern. The interval between the parallel fringes corresponds to b in Fig. 3(a). It is necessary to make the space between fringes as narrow as possible to avoid islands in the fringe pattern. Wide fringes move farther away from the original location than narrower fringes, and as a result, they cover regions, which are considerably different from the optical retardations. This results in the creation of islands [37].
An enlarged view of Part B in Fig. 7(a) is shown in Fig. 7(c), in which the variation of the interferograms caused by the shock cell structures can be observed. The fringe displacements due to the reflected shock waves can also be clearly seen, and these fringes are shifted in a downward direction with the same magnitudes of displacement. Also, it is found that these fringes are not symmetric with respect to the jet centerline; however, we cannot obtain more information on the detailed structures of the microjet from this interferogram alone.
A comparison between the experimental measurement of the density contour plot at the cross-section including the jet centerline and the corresponding numerical result are depicted in Figs. 8 (a) and (b). The contour levels with an interval of 0.1 kg/m^3 are shown at the top, and the spatial

resolution in the experimental density map is around 4 μm. Unlike the interferogram of Fig. 7(a), the density contour plot (Fig. 8(a)) illustrates the various flow features of the shock cell structures quantitatively, such as the shape and size of the expansion and compression regions, the shock cell intervals, the jet boundaries, and the shear layers. Although the unsteady features are ignored here

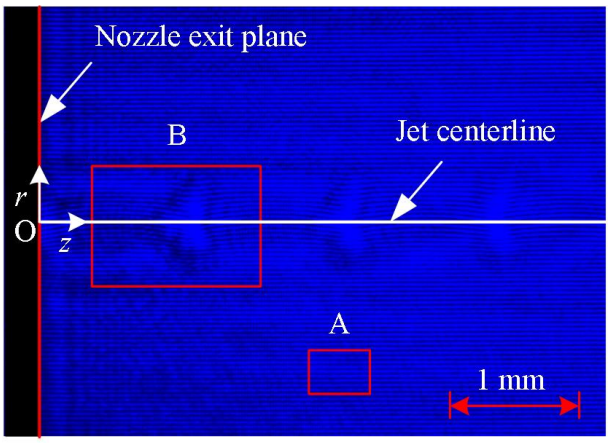

(a) Interferograms of underexpanded sonic jet

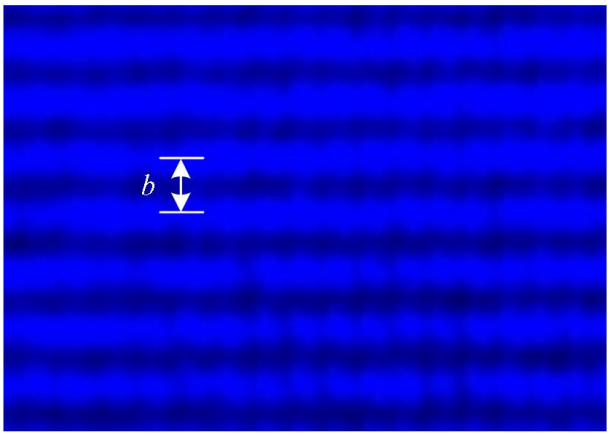

(b) Enlarged view of Part A

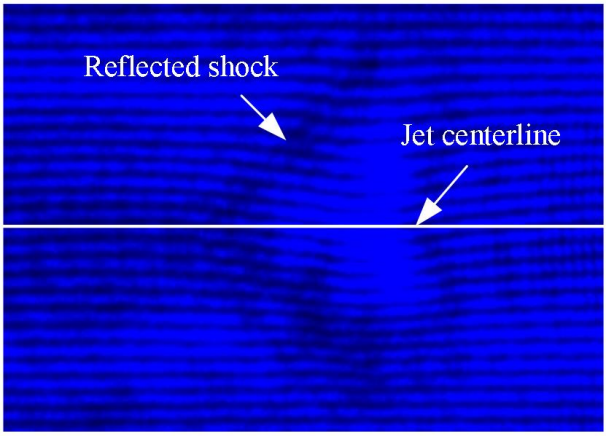

(c) Enlarged view of Part B

Fig. 7. Typical interferograms by wedge fringe method

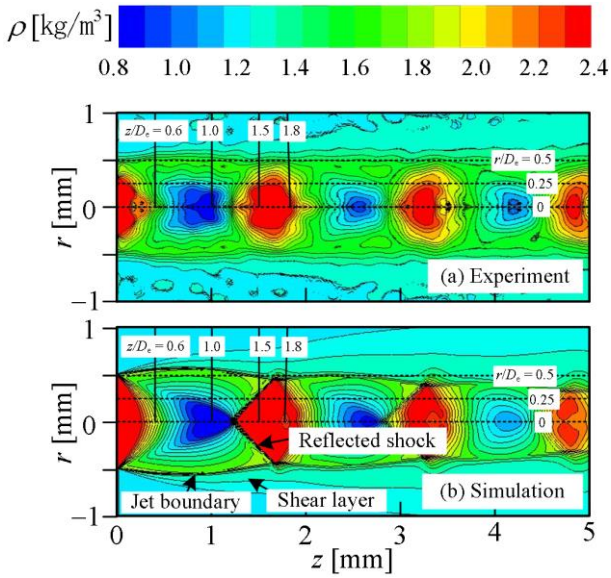

Fig. 8. Density contours of underexpanded microjets

and a relatively coarse mesh is used, there is very favorable overall agreement between the experiment and the simulation on the shock-cell structures; however, the simulation displays a distinct reflected shock when compared with the experiment (see around z = 1~1.5 mm). Also, the experimental data shows that the edge location of the shear layer remains almost the same (r = 0.5 mm) until the end of the domain, but the prediction does not. This discrepancy can be attributed to two issues: first, that axial symmetry is assumed and thus the nature of the fully three-dimensional effects might not be captured, and second, the unsteady features are not captured by this RANS simulation.

These issues should be investigated. Although a Mach disk cannot be recognized in the contour plots for the experiment and simulation of Fig. 8 in this study, Andre et al. [38] showed the presence of a Mach disk with a small diameter in the first shock-cell by the measurement using the particle image velocimetry (PIV). Their experiments were performed under a nozzle pressure ratio of NPR = 3.67 using an axisymmetric convergent nozzle with an inner diameter of 38.7 mm at the nozzle exit. In future studies, we plan to perform a sensitivity analysis against the NPR and the nozzle diameter to characterize a Mach disk in a similar configuration.

Comparisons between the experiment and the simulation for the streamwise density profiles at radial distances of r = 0 mm, 0.25 mm and 0.5 mm are shown in Figs. 9 (a) – (c) where the experimental results are represented with precision error bars. (These radial locations are shown as the three horizontal dotted lines in the contour plots of Fig. 8.) The density value at the nozzle exit plane, which is estimated based on the assumption of the one-dimensional isentropic flow from the nozzle inlet to the exit, is shown as a leftward arrow on the vertical axis as a reference. Also, the solid line parallel to the abscissa indicates the level of the ambient density ρ_b = 1.2 kg/m^3 in the present experiment and simulation. The experimental centerline density profile in Fig. 9 (a) shows a representative distribution appearing in the shock-cell structure in an underexpanded free jet, i.e., the density rapidly decreases below the ambient level by expansion waves originating from the nozzle lip. This shows a sharp increase just downstream of a local minimum at z = around 1.2 mm and then the flow expansion and compression are repeated downstream. The local minima in the density profiles for the experiment and simulation gradually increase with increasing streamwise distance. This trend is in good agreement with the experimental result performed by Panda and Seasholtz [39]. In addition, the simulated density profile exhibits a similar trend as the experiment except that the simulation shows a smooth density variation at the entire streamwise locations

compared with the experiment. This may be due to the overlooked three-dimensional effects, unsteady flow features, and possible inadequacy of the current simulation model (e.g, coarse mesh). However, as can be seen, the overall agreement between the measured and simulated density profiles is favorable from the nozzle exit (z = 0 mm) to the exit of the simulation domain (z = 5 mm). Also, both the predicted shock-cell lengths and density amplitudes agree well with the measurement, except for some spike waveforms present at local maxima and some minor oscillations in the measured curves. A waveform with two distinct spikes (z = around 1.6 and 1.8 mm) just downstream of the density jump caused by a shock in the first shock-cell also seems to appear just downstream of a Mach disk in the density profile obtained from the rainbow schlieren deflectometry by Takano et al [40] as illustrated later in Fig. 12. Additionally, a similar waveform just downstream of a Mach disk can be observed from the velocity profile along the jet centerline obtained by PIV of Andre et al. [38]. However, as shown by a two-way arrow in Fig. 9(a), assuming that density increment at z = around 1.2 mm is responsible for a Mach disk, the estimated density value is significantly lower than those of both the experiment and the simulation. The primary reason could be attributed to the oscillation of the Mach disk position [41 ~ 43]. When the Mach disk oscillates across the time-mean position, the flow Mach number relative to the upstream traveling Mach disk is higher compared to that just ahead of the stationary Mach disk, which results in an excessive density increment in addition to the density jump produced by the Rankine-Hugoniot relations. Figures 9(b) and 9(c) show the measured and simulated density profiles at radial locations of r = 0.25 mm and 0.5 mm, respectively. Again, the overall agreement between the experimental and simulated results is good.

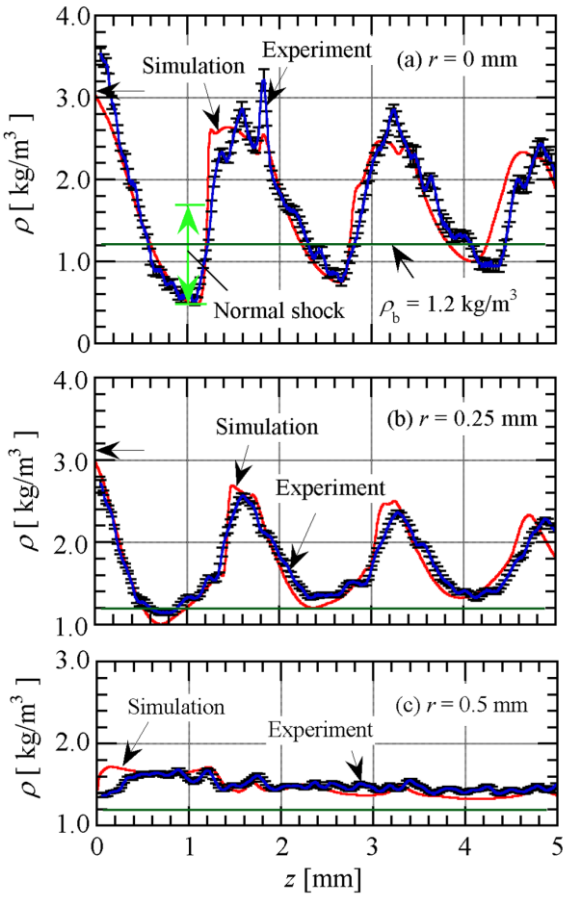

Fig. 9. Streamwise density profiles of underexpanded microjets

Comparisons between the experiment and the simulation for the radial density profiles along the four parallel vertical lines (z = 0.6, 1.0, 1.5 and 1.8 mm) in the density contour plots in Fig. 8 are shown in Figs. 10 (a) - (d). The dashed line indicates the density value estimated based on the assumption that the flow from the nozzle is isentropically expanded to the back pressure, which is referred to as the fully expanded jet density ρ_j and is estimated to be 1.79 kg/m^3 in this experiment. The solid and open circles shown on the experimental and numerical density profiles in Figs. 10 (a) and 10(b) are the radial positions of the local maximum and minimum values, respectively. The maximum density values in the simulated density profiles in both Figs. 10(a) and 10(b) are in quantitatively good agreement with the fully expanded jet density ρ_j and the corresponding radial positions nominally indicate the inviscid jet boundary [39]. The density at the jet boundary approaches the ambient density ρ_b (=1.2 kg/m^3) through the shear layer radially outside of the boundary. It is noted that the ρ_j is different from the ambient density ρ_b even though the fully-expanded jet pressure p_j has to exactly coincide with the back pressure p_b. Therefore, we conclude that the position of the local maximum in the density profile for the experiment seems to correspond to that of the inviscid jet boundary. As shown in Fig. 10(c), the radial density profile passing through the middle of the reflected shock exhibits a noticeable discrepancy between the experimental and simulated results. The experimental density profile is not capable of capturing a reflected shock wave, although the simulated density profile shows that the density remains uniform until it crosses the reflected shock and suddenly drops to the density at the inviscid jet boundary just downstream of the reflected shock. It is followed by a small density peak (r = 0.4 mm), gradually decreasing to the ambient density through the shear layer. In the radial density profiles downstream of the reflected shock shown in Fig. 10(d), relatively good agreement between the experimental and simulated results is achieved, with the exception of the minor density oscillations in the experimental profile.

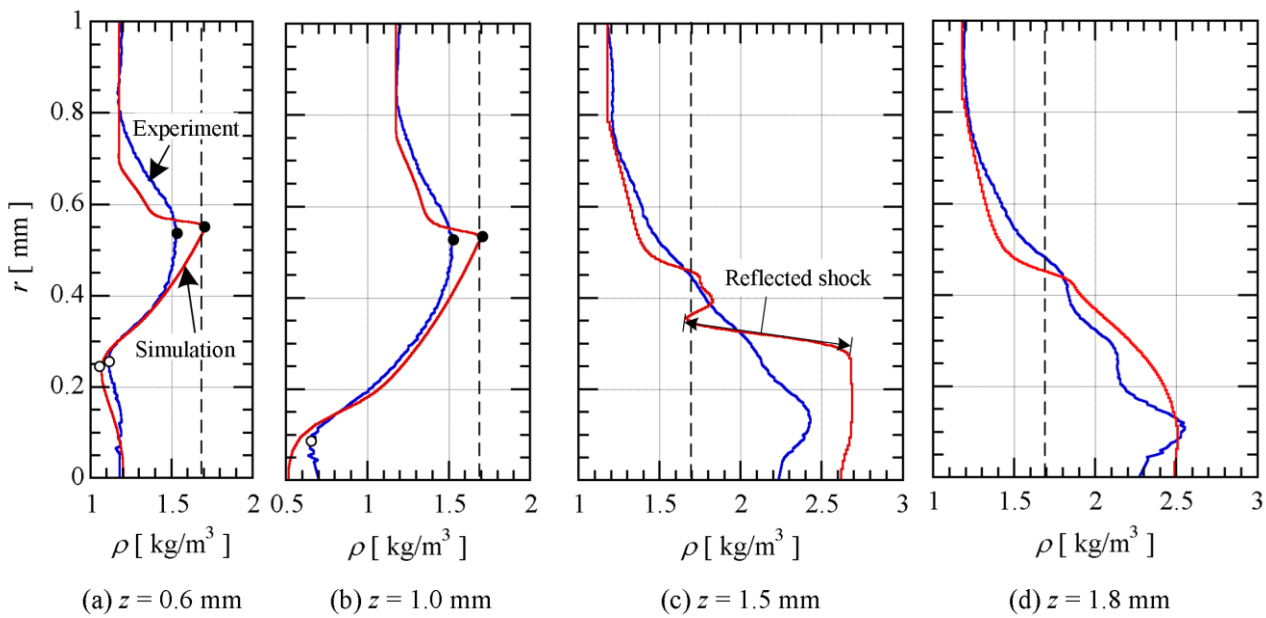

Fig. 10. Comparison between experimental and simulated radial density profiles of underexpanded microjets for NPR = 4.0

Figure 11 shows the radial static pressure profiles along four parallel vertical lines (z/D_e = 0.6, 1.0, 1.5, and 1.8) (see Fig. 8(b)). The horizontal axis is normalized by the back pressure p_b which is the same as the fully-expanded jet pressure p_j. As seen from a comparison between the simulated

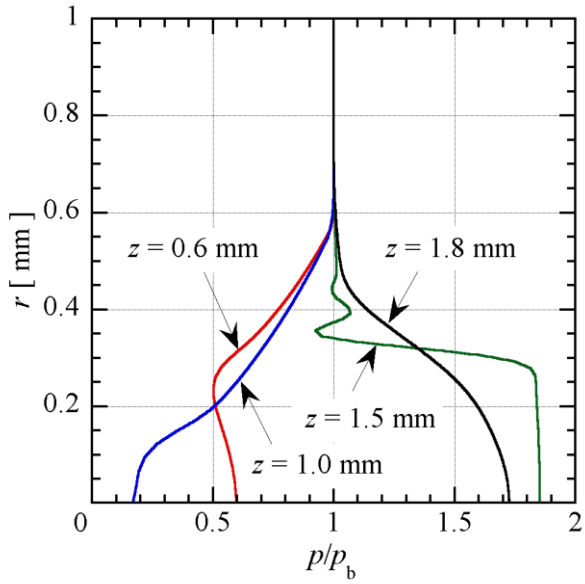

Fig. 11. Radial static pressure profiles obtained from RANS simulation for NPR = 4.0

density and pressure profiles at the corresponding streamwise locations in Figs. 10 and 11, the static pressures coincide with the back pressure p_b at the edge of the inviscid jet boundary indicated by the density profiles at z = 0.6 mm and 1.0 mm. For the density profiles at z = 1.5 mm (Fig. 10 (c)) and 1.8 mm (Fig. 10(d)), for analogical reasons, the radial locations (r = around 0.45 mm), in which the static pressures are equal to p_b, seem to be the inviscid jet boundaries. The static pressure in the jet shear layer is equal to the back pressure at all axial locations. This contrasts with the density at the inviscid jet boundary, which gradually decreases toward the ambient density.

For obtaining density data on shock-containing free jets, various nonintrusive experimental techniques, including rainbow schlieren deflectometry [40, 44, 45], background-oriented schlieren [46 ~ 48], moiré schlieren [49], Mach-Zehnder interferometer [36, 50], Rayleigh scattering [39], coherent anti-Stokes Raman scattering [51], and the dual-hologram interferometry [52], have been presented in the past. However, to the best of our knowledge, comparative studies between density data obtained under the same nozzle shape and experimental conditions are virtually non-existent. Figure 12 shows a comparison between the density profiles along the jet centerline obtained using the various quantitative flow visualization methods for underexpanded sonic jets emitted from the axisymmetric convergent nozzles under the same nozzle operating condition (NPR = 4) with different exit diameters. The density profiles normalized by the ambient density ρ_b from Refs. [40, 48 ~ 50] are superimposed on our measurement (indicated by the blue line) using the Twyman-Green interferometer and the numerical result (indicated by the red line) from the RANS simulation with the SST k-ω turbulent model. In order to make it easier to view, the precision error bars are removed from our experimental result and the theoretical pressure rise by a normal shock wave is also included as a reference. Before comparing the present experimental and simulated results with the past experimental data, it is important to note that the results obtained from the Mach-Zehnder interferometer, the background oriented schlieren, and the rainbow schlieren include a Mach disk in the first shock-cell, while those from the Twyman-Green interferometer, the moiré schlieren and the simulation seem to include an oblique shock instead of a Mach disk. In addition, each methodology relies on certain assumptions and restrictions. The data acquired from the Abel inversion method is based on the assumption of an axisymmetric jet for the Mach-Zehnder interferometer. For the moiré and rainbow schlieren methods, the data measured by the computed tomography with multi-viewing

schlieren pictures are obtained by rotating a test nozzle around its longitudinal axis in equal intervals. Finally, the instantaneous density field reconstructed three-dimensionally with the simultaneous schlieren pictures is taken by mounting 12 synchronized cameras around a test nozzle for the background oriented schlieren.

As seen in Fig. 12, there is good quantitative agreement between the density profile obtained from the Twyman-Green interferometer and those from both the Mach-Zehnder interferometer and the moiré schlieren. The streamwise locations of the first and second local minima showing the ends of the expansion regions in the first and second shock-cells, respectively, and that of the second local maximum showing the end of the compression region in the second shock-cell, and the density values at their corresponding local minima and maximum, agree extremely well. In addition, the density behind an oblique shock wave or a Mach disk in the first shock-cell for each density profile is almost the same peak value regardless of whether a Mach disk is present or not. The density profiles obtained from both the rainbow schlieren and the background schlieren show good quantitative agreement with the simulation with the exception of the density values around the streamwise locations of the local maxima in the density profile. The principal difference between the experiments and the simulation seems to be due to the fact that the experiments include a Mach disk in the jet plume, whereas the simulation does not. It should be noted that Takano et al. used a nozzle configuration that is geometrically similar to that shown in Fig. 2. However, Nicolas et al. [48] utilized the nozzle so that the wall contour is converged in the downstream direction at a constant half angle of 30 deg and followed by a short straight duct to provide a uniform sonic condition on the jet exit plane. What needs to be emphasized here is that there is still room for reconsidering not only the notable difference for the density profile behind a Mach disk, but also an additional density increment after the theoretical density jump by the normal shock wave.

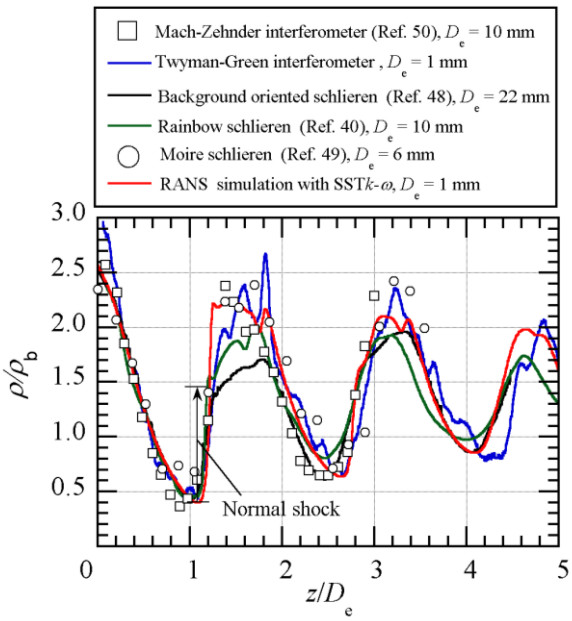

Fig. 12. Comparison between centerline density profiles of underexpanded sonic jets obtained by various nonintrusive methods for NPR = 4.0

6 Concluding Remarks

In the present study, the Twyman-Green interferometer was applied for the first time to "quantitatively" measure the density profiles over the whole flow field of shock-containing microjets quantitatively. In this experiment, a nozzle pressure ratio was set to 4.0, which produces

an underexpanded free jet. The microjet structures were experimentally measured and demonstrated not only in the density contour plot at the cross-section including the jet centerline, but also in the streamwise and radial density profiles. In addition, the RANS simulation with the SST k-ω turbulent model was performed with the intent of a mutual comparison with the present experiment and to clarify the fine spatial features of the microjet structures. It is shown that the experimental density contour plot illustrates the various flow features of the microjet, including the shape and size of the expansion and compression regions, the shock cell intervals, the jet boundaries, and the shear layers. Very favourable overall agreement between the experiment and the simulation on the global shock-cell structures is achieved. More specifically, an excellent quantitative agreement is achieved between the experiment and the simulation for the streamwise density profiles. Both the simulated shock-cell lengths and density amplitudes are consistent with the measurement, except for some spike waveforms present at the local maxima and some minor oscillations in the measured curves. From comparisons between the experiment and the simulation of the radial density profiles across a reflected shock wave in the first shock-cell, we can recognize the radial locations of the inviscid jet boundaries inside the shear layer. In the radial density profiles downstream of the reflected shock, the agreement between the experimental and the simulated results is not excellent, but satisfactory. In the experimental density profile, the flow feature of the reflected shock wave shown in the simulation is missing.

The jet centerline density profile obtained from the present study was quantitatively compared with those from past studies such as the rainbow schlieren deflectometry, the background oriented schlieren, the moiré schlieren, and the Mach-Zehnder interferometer. The centerline density profiles in underexpanded jets emitted from the axisymmetric convergent nozzles for the same nozzle pressure ratio were demonstrated to investigate the effects of the nozzle exit diameters as well as how different measuring techniques work. It is found that the density profiles obtained from the Twyman-Green interferometer, the Mach-Zehnder interferometer and the moiré schlieren are in good quantitative agreement with each other. It is also shown that the simulated result agrees well with those obtained from the rainbow schlieren and the background schlieren except for the density variation downstream of a shock wave in the first shock-cell. At this stage, we cannot make firm conclusions about what causes the significant discrepancies seen in the density values just behind a shock wave in the first shock-cell among the experiments, the simulations, and normal shock theory. To elucidate the local phenomena at a higher level of complexity on shock dynamics, further experimental studies using more sophisticated instrumentation or high fidelity numerical models (e.g., LES, DNS, etc.) using a very fine mesh may be necessary. The present study is the first trial of its kind among applications of the Twyman-Green interferometers for supersonic microjets, and it shows that the Twyman-Green interferometer proves to be a very efficient tool to investigate the fine structures of shock-containing microjets at a high spatial resolution. The present experimental and numerical results could be useful for the validation of various numerical simulation codes for the case of shock-containing free jets under precisely identical operating conditions and nozzle configurations.

7 Acknowledgements

This work was in part funded by Grant-in-Aid for Scientic Research (C) No. 15K05804 of Japan Society for the Promotion of Science. The authors are grateful to graduate students Takashi Muranaka and Teppei Goto of our laboratory for their assistance in the experimental work. The authors also wish to express our deepest thanks to Dr. Daisuke Ono for the development of the software for reconstruction of the density field from interference images. Without his persistent help this research would not have been possible. Thanks are offered to Engineering Advisor Hiroyuki Ohtsubo of the Machine Shop in the University of Kitakyushu for his technical support on image processing systems. In addition, the authors would like to thank Dr. Zensho Nakao (Professor

Emeritus, University of the Ryukyus) for proofreading of this manuscript. The present paper has been refined in accordance with his review. Finally, the authors would like to dedicate a special thanks to Dr. Kenji Miki for his invaluable comments on this manuscript as well as precise suggestions on the numerical simulation. It was our great honor that we met him at ISABE2017. He continues to be a source of encouragement for our laboratory.

References

[1] Bayt R. and Breuer K., Systems design and performance of hot and cold supersonic microjets, *AIAA Paper*, No. 2001-0721, 2001.
[2] Nakao S., and Takamoto M., Choking phenomena of sonic nozzles at low Reynolds numbers, *Flow Measurement and Instrumentation*, 11-4, pp 285-291, 2000.
[3] Louisos W.F., and Hitt D.L., Heat transfer & viscous effects in 2D & 3D supersonic micro-nozzle flows, *AIAA Paper*, No. 2007-3987, 2007.
[4] Scroggs S.D., and Settles G.S., An experimental study of supersonic microjets, *Experiments in Fluids*, 21, pp 401-409, 1996.
[5] Phalnikar K.A., Kumar R., and Alvi F.S., Experiments on free and impinging supersonic microjets, *Experiments in Fluids*, 44-5, pp 818-830, 2008.
[6] Aniskin V., Mironov S., and Maslov A., Investigation of the structure of supersonic nitrogen microjets, *Microfluid Nanofluid*, 14, pp 605-614, 2013.
[7] John J. E. A., *Gas dynamics.* 2nd edition, Allyn and Bacon, INC., p 352, 1984.
[8] Koike S., Suzuki K., Kitamura E., Hirota M., Takita K., Masuya G., and Matsumoto M., Measurement of vortices and shock waves produced by ramp and twin jets, *J. Propulsion and Power*, 22-5, pp 1059-1067, 2006.
[9] Huffman, Jr. R. E., and Elliott G. S., An experimental investigation of accurate particle tracking in supersonic, rarefied axisymmetric jets, *AIAA Paper*, No. 2009-1265, 2009.
[10] Wernet M. P., Application of tomo-PIV in a large-scale supersonic jet flow facility, *Experiments in Fluids*, 57:144, 2016.
[11] Pack D.C., A note on Prandtl's formula for the wave-length of a supersonic gas jet, *Quarterly Journal of Mechanics and Applied Mathematics*, 3-2, pp 173-181, 1950.
[12] Tam C.K.W., On the noise of a nearly ideally expanded supersonic jet, *J. Fluid Mechanics*, 51-1, pp 69-95, 1972.
[13] Tam C.K.W., Jackson J.A., and Seiner J.M., A multiple-scales model of the shock-cell structure of imperfectly expanded supersonic jets, *J. Fluid Mechanics*, 153, pp 123-149, 1985.
[14] Tam C.K.W., The shock-cell structures and screech tone frequencies of rectangular and non-axisymmetric supersonic jets, *J. Sound and Vibration*, 121-1, pp 135-147, 1988.
[15] Morris P.J., Bhat T.R.S., and Chen G., A linear shock cell model for jets of arbitrary exit geometry, *J. Sound and Vibration*, 132-2, pp 199-211, 1989.
[16] Emami B., Bussmann M., and Tran H. N., A mean flow field solution to a moderately under/over-expanded turbulent supersonic jet, C.R. *Mecanique*, 337, pp 185-191, 2009.
[17] Chin C., Li M., Harkin C., Rochwerger T., Chan L., Ooi A., Risborg A., and Soria J., Investigation of the flow structures in supersonic free and impinging jet flows, *Transactions of the ASME*, *J. Fluids Engineering*, 135, 031202-1, 12. 2013.
[18] Franquet E., Perrier V., Gibout S., and Bruel P., Free underexpanded jets in a quiescent medium: A review. *Progress in Aerospace Sciences*, 77, pp 25-53, 2015.
[19] Miller S. A. E., Veltin J., Morris P. J., and McLaughlin D. K., 2009 Assessment of computational fluid dynamics for supersonic shock containing jets. *AIAA J.*, 47-11, pp 2738-2746, 2009.
[20] Liu J., Kailasanath K., Ramamurti R., Munday D., Gutmark E., and Lohner R., Large-eddy simulations of a supersonic jet and its near-field acoustic properties, *AIAA J.*, 47-8, pp 1849-1864, 2009.
[21] Emami B., Bussmann M., and Tran H., Application of realizability and shock unsteadiness to k-ε simulations of under-expanded axisymmetric supersonic free jets, *Transactions of the ASME*, *J. Fluids Engineering*, 132, 041104, 2010.
[22] Settles G.S., *Schlieren and schadowgraph techniques: visualizing phenomena in transparent media*, Springer-Verlag, 2001.
[23] Loh C. Y., and Hultgren L. S., Jet screech noise computation. *AIAA J.*, 44-5, pp 992-998, 2006.
[24] Li X., Yao W., and Fan X., Large-eddy simulation of time evolution and instability of highly underexpanded sonic jets, *AIAA J.*, 54-10, pp 3191-3211, 2016.
[25] Li X., Zhou R., Yao W., and Fan X., Flow characteristic of highly underexpanded jets from various nozzle geometries, *Applied Thermal Engineering*, 125, pp 240-253, 2017.
[26] Born M. and Wolf E., *Principles of optics*, Cambridge University Press, 7th (expanded) edition, pp 336-341, 2011.

[27] Takeda M., Ina H., Kobayashi S., Fourier-transform method of fringe-pattern analysis for computer-based topography and interferometry, *Journal of the Optical Society of America*, 72-1, pp 156-160, 1982.
[28] Nestor O.H., and Olsen H.N., Numerical methods for reducing line and surface probe data, *SIAM Review*, 2-3, pp 200-207, 1960.
[29] Smits A.J., and Lim T.T., *Flow visualization: techniques and examples*, Imperial College Press, pp 226-230, 2000.
[30] Yagi S., Inoue S., Nakao S., Ono D., and Miyazato Y., Optical measurements of shock waves in critical nozzles at low Reynolds numbers, *Journal of Flow Control, Measurement & Visualization*, 5-2, pp 36-50, 2017.
[31] Sneddon I. N., *The use of integral transforms*, McGraw-Hill Book Company, p 318, 1972.
[32] Bradley J.W., Density determination from axisymmetric interferograms, *AIAA J.*, 6-6, pp 1190-1192, 1968.
[33] Behjat A., Tallents G.J., and Neely D., The characterization of a high-density gas jet, *J. Physics*, D: *Applied Physics*, 30, pp 2872-2879. 1997
[34] Malka V., Coulaud C., Geindre J. P., Lopez V., Najmudin Z., Neely D., and Amiranoff F., Characterization of neutral density profile in a wide range of pressure of cylindrical pulsed gas jets, *Review of Scientific Instruments*, 71-6, pp 2329-2333, 2000.
[35] Álvarez, R., Rodero, A., Quintero, M.C., An Abel inversion method for radially resolved measurements in the axial injection torch, *Spectrochimica Acta*, Part B, 57, pp 1665-1680, 2002.
[36] Shimomiya, K., Ono, D., and Miyazato, Y., Mach-Zehnder interferogram analysis of axisymmetric underexpanded sonic jet using Fourier-Hankel methods, *51st AIAA Aerospace Sciences Meeting including the New Hrizons Forum and Aerospace Exposition*, Grapevine, Texas, No. 2013-0230, 2013.
[37] Winckler J., The Mach interferometer applied to studying an axially symmetric supersonic air jet, *The Review of Scientific Instruments*, 19-5, pp 307-322, 1948.
[38] André B., Castelain T., and Bailly C., Investigation of the mixing of underexpanded supersonic jets by particle image velocimetry, *International Journal of Heat and Fluid Flow*, 50, pp 188-200, 2014.
[39] Panda J., and Seasholtz R. G., Measurement of shock structure and shock-vortex interaction in underexpanded jets using Rayleigh scattering, *Physics of Fluids*, 11-12, pp 3761-3777, 1999.
[40] Takano H., Kamikihara D., Ono D., Nakao S., Yamamoto H., and Miyazato Y., Three-dimensional rainbow schlieren measurements in underexpanded sonic jets from axisymmetric convergent nozzles, *J. Thermal Science*, 25-1, pp 78-83, 2016.
[41] Di Rosa M.D., Chang A.Y., Hanson R.K., Continuous wave dye-laser technique for simultaneous, spatially resolved measurements of temperature, pressure, and velocity of NO in an underexpanded free jet, *Applied Optics*, 32-21, pp 4074-4087, 1993.
[42] Panda J., Shock oscillation in underexpanded screeching jets, *J. Fluid Mechanics*, 363, pp 173-198, 1998.
[43] Edgington-Mitchell D., and Honnery D. R., and Soria J., The underexpanded jet Mach disk and its associated shear layer, *Physics of Fluids*, 26, 096101, 2014.
[44] Satti R.P., Kolhe P.S., Olcmen S., Agrawal A.K., Miniature rainbow schlieren deflectometry system for quantitative measurements in microjets and flames, *Applied Optics*, 46-15, pp 2954-2962, 2007.
[45] Kolhe P. S. and Agrawal A. K., Density measurements in a supersonic microjet using miniature rainbow schlieren deflectometry, *AIAA J.*, 47-4, pp 830-838, 2009.
[46] Venkatakrishnan L., Density measurements in an axisymmetric underexpanded jet by background-oriented schlieren technique, *AIAA J.*, 43-7, pp 1574-1579, 2005.
[47] Van Hinsberg N.P. and Rosgen T., Density measurements using near-field background-oriented schlieren, Experiments in Fluids, 55:1720, DOI 10.1007/s00348-014-1720-x, 2014.
[48] Nicolas F., Donjat D., Léon O., Le Besneris G., Champagnat F., and Micheli F., 3D reconstruction of a compressible flow by synchronized multi-camera BOS, *Experiments in Fluids*, 58:46, DOI 10.1007/s00348-017-2325-y, 2017.
[49] Tabei K., Shirai H., and Takakusagi F., Density measurements of underexpanded free jets of air from circular and square nozzles by means of moiré-schlieren method, *JSME International Journal*, Series II, 35-2, pp 212-217, 1992.
[50] Nakamura T, and Iwamoto J., A quantitative analysis of axisymmetric flow with shock waves from interferogram, Proceedings of the 4th Asian Symposium on Visualization, Edited by Wei, Q.D., *International Academic Publishers*, , pp 235-240, 1996.
[51] Woodmansee I. V., Dutton J. C., and Lucht R.P., Nonintrusive pressure and temperature measurements in an underexpanded sonic jet flowfield. *AIAA J.*, 42-6, pp 1170-1180, 2004.
[52] Velasquez-Aguilar J. G., Toker G., Zamudio-Lara A., and Arias-Estrada M., Visualization of a supersonic air micro jet by methods of dual-hologram interferometry, *Experiments in Fluids*, 42, pp 863-869, 2007.